APL Materials

Role of intermediate *4f* states in tuning the band structure of high entropy oxides

Cite as: APL Mater. **8**, 051111 (2020); https://doi.org/10.1063/5.0007944
Submitted: 17 March 2020 . Accepted: 21 April 2020 . Published Online: 19 May 2020

Abhishek Sarkar, Benedikt Eggert, Leonardo Velasco, Xiaoke Mu, Johanna Lill, Katharina Ollefs, Subramshu S. Bhattacharya, Heiko Wende, Robert Kruk, Richard A. Brand, and Horst Hahn

Role of intermediate 4*f* states in tuning the band structure of high entropy oxides

Cite as: APL Mater. 8, 051111 (2020); doi: 10.1063/5.0007944
Submitted: 17 March 2020 • Accepted: 21 April 2020 •
Published Online: 19 May 2020

View Online Export Citation CrossMark

Abhishek Sarkar,[1,2,a] Benedikt Eggert,[3] Leonardo Velasco,[2] Xiaoke Mu,[2] Johanna Lill,[3] Katharina Ollefs,[3] Subramshu S. Bhattacharya,[4] Heiko Wende,[3] Robert Kruk,[2] Richard A. Brand,[2,3] and Horst Hahn[1,2,b]

AFFILIATIONS

[1]Joint Research Laboratory Nanomaterials – Technische Universität Darmstadt and Karlsruhe Institute of Technology, Otto-Berndt-Str. 3, 64287 Darmstadt, Germany
[2]Institute of Nanotechnology, Karlsruhe Institute of Technology, Hermann-von-Helmholtz-Platz 1, 76344 Eggenstein-Leopoldshafen, Germany
[3]Faculty of Physics and Center for Nanointegration Duisburg-Essen (CENIDE), University of Duisburg-Essen, Lotharstr. 1, 47057 Duisburg, Germany
[4]Nano Functional Material Technology Centre (NFMTC), Department of Metallurgical and Materials Engineering, Indian Institute of Technology Madras, 600036 Chennai, India

[a]**Author to whom correspondence should be addressed:** abhishek.sarkar@kit.edu
[b]**Electronic mail:** horst.hahn@kit.edu

ABSTRACT

High entropy oxides (HEOs) are single-phase solid solutions consisting of 5 or more cations in approximately equiatomic proportions. In this study, we show the reversible control of optical properties in a rare-earth (RE) based HEO-$(Ce_{0.2}La_{0.2}Pr_{0.2}Sm_{0.2}Y_{0.2})O_{2-\delta}$ and subsequently utilize a combination of spectroscopic techniques to derive the features of the electronic band structure underpinning the observed optical phenomena. Heat treatment of the HEO under a vacuum atmosphere followed by reheat treatment in air results in a reversible change in the bandgap energy, from 1.9 eV to 2.5 eV. The finding is consistent with the reversible changes in the oxidation state and related *f*-orbital occupancy of Pr. However, no pertinent changes in the phase composition or crystal structure are observed upon the vacuum heat treatment. Furthermore, annealing of this HEO under a H_2 atmosphere, followed by reheat treatment in air, results in even larger but still a reversible change in the bandgap energy from 1.9 eV to 3.2 eV. This is accompanied by a disorder–order type crystal structure transition and changes in the O 2*p*–RE 5*d* hybridization evidenced from x-ray absorption near-edge spectra (XANES). The O *K* and RE $M_{4,5}/L_3$ XANES indicate that the presence of Ce and Pr (in 3+/4+ states) leads to the formation of intermediate 4*f* energy levels between the O 2*p* and the RE 5*d* gap in HEO. It is concluded that heat treatment under reducing/oxidizing atmospheres affects these intermediate levels, thus offering the possibility to tune the bandgap energy in HEOs.

I. INTRODUCTION

High entropy oxides (HEOs) were first reported in 2015,[1] and since then the topic has gained significant interest, which is evident from numerous published reports focusing on different aspects of HEOs.[2–10] HEOs can be broadly defined as single-phase solid solution oxides containing 5 or more cations in near-equiatomic compositions. The presence of multiple cations in comparable amounts leads to an enhanced configurational entropy of mixing (S_{config}), which is calculated using the Boltzmann statistical entropy equation.[1,3,11] The term "high entropy oxide" is typically used when the S_{config} of a given oxide system is above 1.5 R.[3,5,6,12] One of the most intriguing characteristics of HEOs is the phase purity despite their compositional complexity. Interestingly, the underlying principle for phase purity is distinct in different HEOs. For instance, in some systems a dominant role of entropy has been evidenced, which

effectively overcomes the related enthalpic penalties and stabilizes a single-phase solid solution at high temperatures.[1,13,14]

However, in the majority of HEOs a pertinent role of configurational entropy in stabilizing the phase composition and structure has not been observed, whereas factors such as the oxidation states of specific cations and lattice strain effects govern their phase composition.[3,5,6,15,16] Irrespective of the phase stability mechanisms, the high entropy based design approach in oxides offers an extended compositional flexibility along with retention of the phase purity. Hence, compositions close to the central regions of multi-component oxide phase diagrams can be studied, where interesting synergies can be anticipated. A wide range of crystal structures and functional features exhibited by HEOs can be linked to their unique composition and related synergies.[4,6–10,17–24] Nevertheless, disentangling the role of individual elements is one of the major challenges in HEOs.

In our previous studies, we have explored the possibility to synthesize several single-phase fluorite type HEOs (F-HEOs) by populating the cationic sublattice with 5 or more rare-earth (RE) elements.[15,25] By comparing these compositions, we have observed that the presence of Pr in F-HEOs results in a lowering of the bandgap energy. Hence, we speculated that Pr due to its mixed 3+/4+ oxidation state in F-HEOs forms an intermediate unoccupied energy state, which facilitates lower energy electronic transitions of ~2 eV.[25] Understanding the electronic band structure of conventional binary rare-earth oxides is still a subject of both theoretical and practical interest.[26–28] However, the theoretical band structure calculations for complex F-HEOs are not straightforward. Hence, in this current study, we use different spectroscopic techniques to investigate the validity of our hypothesized energy band diagram in a representative F-HEO composition, $(Ce_{0.2}La_{0.2}Pr_{0.2}Sm_{0.2}Y_{0.2})O_{2-\delta}$. Initially, by means of heat treatment under reducing (vacuum/hydrogen) or oxidizing atmospheres, we have observed reversible changes in bandgap energies. The changes in the oxidation states of the RE elements and related variations in the *f* and *d* electronic shell occupancy are studied using x-ray absorption spectroscopy (XAS) and electron energy loss spectroscopy (EELS), which primarily indicates the role of internal redox reactions in determining the electronic characteristics of F-HEOs. Although this kind of redox reaction driven bandgap tuning mechanism is known for simple metal oxides,[29,30] such a possibility has not yet been explored for HEOs. Furthermore, the accompanying physico-chemical changes such as large concentrations of oxygen vacancies, reversible disorder–order transition, and Raman features upon H_2-treatment make the F-HEO different. Hence, this study not only elucidates the dynamic band structure of the F-HEO but also provides a deeper structural insight into these compositionally complex systems.

II. EXPERIMENTAL

A. Synthesis

The F-HEO, $(Ce_{0.2}La_{0.2}Pr_{0.2}Sm_{0.2}Y_{0.2})O_{2-\delta}$, was synthesized from water-based precursor solutions of the corresponding rare-earth nitrates using reverse co-precipitation (RCP) techniques. The precursor solution was added to a basic ammonia solution (pH = 10) in a controlled fashion along with continuous stirring of the mixture at ambient conditions. The formed precipitates were dried at 120 °C and further calcined at 750 °C in air to achieve the desired crystallographic phase. The temperature, 750 °C, has been determined based on the reports of the F-HEO synthesized by the nebulized spray pyrolysis method.[15] The powders obtained after this first 750 °C heat-treatment step in air are defined as the as-synthesized ("as-syn") samples. The as-synthesized samples were subsequently heat treated under different atmospheres, where the temperature, dwell time, and ramping rates (for both heating and cooling) were 750 °C, 2 h, and 10 °C/min, respectively. The heat-treatment conditions were as follows:

- Mildly reducing atmosphere: Vacuum heat treatment (VHT), corresponding to 10^{-7} mbar pressure.
- Highly reducing atmosphere: Heat treatment with flow of a 5% hydrogen–argon mixture (H_2-HT), with a gas flow rate of 50 standard liters per minute.
- Re-heat treatment under air: This was carried out after the VHT or H_2-HT, using the respective VHT/H_2-HT powder. Hence, the samples obtained are termed as RHT (meaning "re-heat treated" in air).

B. Structural and electronic characterization

All the measurements were performed at room temperature, if not stated otherwise.

1. **X-ray diffraction (XRD)**: XRD patterns were recorded using a Bruker D8 Advance diffractometer with the Bragg–Brentano geometry equipped with an x-ray tube having a Cu anode and a Ni filter. The Rietveld analysis of the XRD patterns was done using TOPAS V.5.0.[31] The instrumental intensity distributions were determined using a reference scan of LaB_6 (NIST 660a).
2. **High resolution transmission electron microscopy (HR-TEM), energy dispersive x-ray spectroscopy (EDS), and electron energy loss spectroscopy (EELS)**: Specimens for TEM were prepared by directly dispersing the finely ground powders onto a standard carbon coated copper grid. A FEI Titan 80–300 aberration (imaging Cs) corrected transmission electron microscope equipped with a Gatan Tridiem 863 image filter operated at 300 kV was used to examine the specimens. EELS spectra were collected in the TEM mode (an objective aperture of 30 μm, a convergence semi-angle of <0.5 mrad, a dispersion of 0.1 eV/channel, a collection semi-angle of 15 mrad, and an acquisition time of 5 s) and in the scanning TEM (STEM) mode (a condenser aperture of 70 μm, a convergence semi-angle of 14 mrad, a dispersion of 0.1 eV/channel, a collection semi-angle of 16 mrad, and an acquisition time of 5 s). EDS maps were collected in the STEM mode.
3. **Ultraviolet-visible (UV-Vis) spectroscopy**: The UV-Vis spectra were recorded in the diffuse reflectance mode in the range from 200 nm to 1200 nm using a PerkinElmer Lambda 900 spectrophotometer. From the obtained spectra, optical bandgaps were determined by applying the Tauc relation,[32]

$$[F(R_\infty)h\nu]^{1/n} = A(h\nu - E_g),$$

where $F(R_\infty)$ is the Kubelka–Munk function, h is Planck's constant, ν is the incident frequency, A is a constant, and E_g is the bandgap energy. The exponent n denotes the nature of the

optical transitions. In this study, $n = 1/2$ has been used, which is valid for direct allowed transitions. The bandgap energy values were calculated from linear regression at the inflection point of the $[F(R_\infty)h\nu]^2$ vs hν (Tauc) plots. The obtained $h\nu$-intercept values were taken as the bandgap values.

4. **Raman spectroscopy**: Raman spectra were recorded using a Renishaw Raman microscope using the infrared (785 nm) laser and green (532 nm) laser in the range of 200–2000 cm^{-1}, with a spot size of ~1 μm and a laser power of 0.5 mW. All the spectra were the result of 10 accumulations, each lasting 20 s.
5. **X-ray absorption spectroscopy (XAS)**: XAS was utilized to study the valence states and the chemical environment of different constituents. For the investigation of the RE 4*f* and O 2*p* states, measurements were performed in the soft x-ray regime at the XUV diffractometer endstation, located at the beamline UE46_PGM-1[33] (BESSY II, Berlin), while for the investigation of the RE 5*d* states, measurements in the hard x-ray regime were performed at the beamline P65[34] (PETRA III, Hamburg). Due to the large difference of the used photon energy, different measurement procedures were used. For the (room temperature) measurements in the soft x-ray regime (O 2*p* and RE 4*f* states), the sample powder was pressed into indium foil to ensure electrical grounding, while the signal was measured in total electron yield (TEY). In the hard x-ray regime (RE-5*d* edges), the sample powder was pressed into a pellet, while the absorption measurements were performed in the transmission mode at 10 K. Because of the presence of many atomic species in these samples, careful subtraction of the background signal was necessary. More fundamentally, because of the computational difficulty in calculating the near-edge spectra from first principles in these complex mixed oxides, we have restricted our analysis here to a description of individual white line changes and comparisons with well established literature results. A recent review of the possibilities of XANES studies has been given by Henderson *et al.*[35] and in a larger context by Wende.[36]

III. RESULTS

The results obtained for heat treatment of $(Ce_{0.2}La_{0.2}Pr_{0.2}Sm_{0.2}Y_{0.2})O_{2-\delta}$-F-HEO in vacuum differ significantly to those obtained when heat-treated in a hydrogen atmosphere. Hence, two subsections specific to the heat-treating atmosphere are made.

A. Vacuum heat treatment

1. Changes in the optical properties upon VHT

The as-synthesized F-HEO powder has been subjected to vacuum heat treatment (VHT) followed by subsequent re-heat treatment (RHT) in air. An immediate indication of a reversible change can be observed by simple inspection of the powder color, as shown in Figs. 1(a)–1(c). The as-synthesized powder is dark brown in color [Fig. 1(a)], whereas VHT leads to a yellow powder [Fig. 1(b)], and upon further RHT, the initial brown color [Fig. 1(c)] is regained. Likewise, the diffuse reflectance spectra of the powders support this observation, and the corresponding changes in the bandgap energies have been estimated, as presented in Fig. 1(d). The bandgap energy of the as-synthesized powder is 1.93 eV. Upon VHT, an increase in the bandgap to 2.47 eV can be observed. The RHT of the powder in air leads to a reversal of the bandgap to 1.98 eV. This value is close to the bandgap of the as-synthesized system, and the difference (~5%) falls within the experimental error of the measurement.

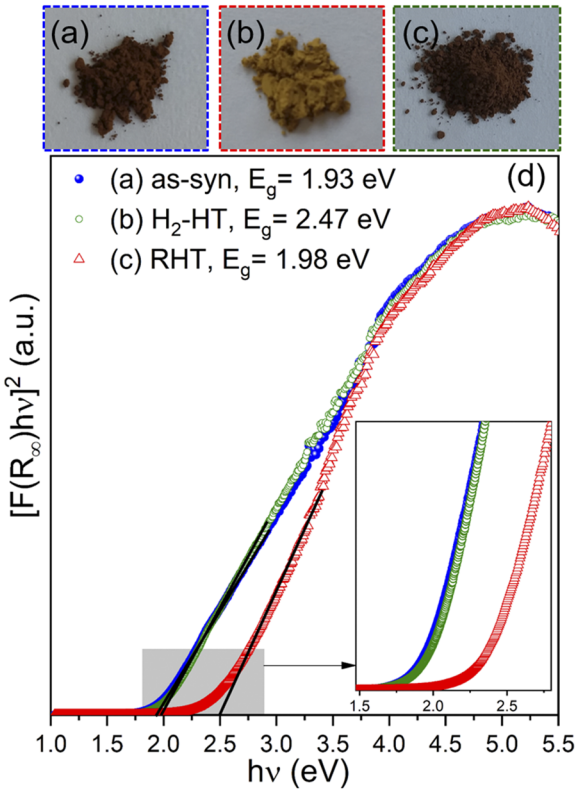

FIG. 1. Photographs of the $(Ce_{0.2}La_{0.2}Pr_{0.2}Sm_{0.2}Y_{0.2})O_{2-\delta}$ powder, where (a) is the as-synthesized powder, (b) VHT, and (c) RHT after the VHT. (d) The corresponding Tauc plot obtained from the UV-Vis spectra of these powders confirms reversible tuning of the bandgap. The bandgap values are within the 5% error bar, i.e, ±0.1 eV.

2. Structural analysis and phase composition upon VHT

One of the main characteristics of HEOs is their phase purity; hence, it is important to investigate the effect of heat treatment on the phase composition of F-HEOs. Figure 2 presents the XRD patterns, HR-TEM micrographs, and selected area electron diffraction (SAED) patterns of the as-synthesized, VHT, and RHT samples. HR-TEM micrographs along with the XRD patterns reveal the presence of nano-sized crystallites, which aggregate to form micron sized particles. Structural details obtained from Rietveld refinement of the XRD patterns are presented in supplementary material, Fig. SI1. Importantly, no change in the crystal structure, phase composition, or elemental distribution (supplementary material, Fig. SI2) can be observed upon heat treatment under varying atmospheres. A marginal increase in the lattice parameter (~0.4%, see Table I) along with broadening of the peaks due to strain effects can

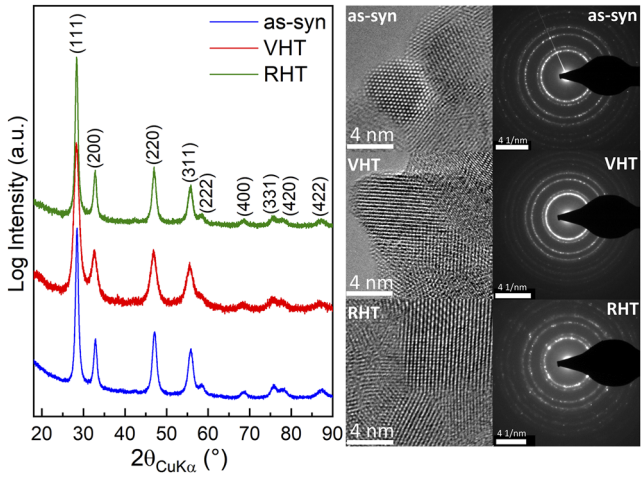

FIG. 2. XRD patterns confirming the phase purity of as-synthesized, vacuum heat treated (VHT), and air re-heat treated (RHT) F-HEOs. The TEM micrographs are in good agreement with the XRD results, confirming the nanocrystallinity and phase purity at the local level.

be observed upon VHT (Fig. 2). These observations hint toward the reduction in some of the constituent cations (resulting in larger ionic sizes) and related oxygen vacancy formation, which is the focus of Subsection III A 3.

3. Oxidation state and charge compensation upon VHT

In our previous report,[25] we inferred that the bandgap energy of ~2 eV in F-HEOs is closely associated with the presence of multivalent Pr^{3+}/Pr^{4+}. Following this speculation, it can be expected that the change/reduction in the oxidation state of Pr will affect the occupancy of the Pr 4*f* states. Hence, a change in the bandgap energy of F-HEOs can be expected. In order to investigate the change in the oxidation of constituent elements upon VHT, EELS measurements have been carried out.

TABLE I. Summary of the lattice parameter (*a*) and direct bandgap energy (E_g) values of $(Ce_{0.2}La_{0.2}Pr_{0.2}Sm_{0.2}Y_{0.2})O_{2-\delta}$ heat treated under different conditions. The *a* of bixbyite ($Ia\bar{3}$) should be divided by 2 to obtain the pseudosymmetric lattice parameter, which is needed for comparison purposes.

Heat treatment	Crystal structure	*a* (Å)	E_g (eV)[a]
As-syn (750 °C-air)	$Fm\bar{3}m$	5.4782(5)	1.93
1000 °C-air	$Ia\bar{3}$[b]	10.9632(5)	2.03
750 °C, VHT	$Fm\bar{3}m$	5.5035(4)	2.47
750 °C, VHT+RHT	$Fm\bar{3}m$	5.4832(4)	1.98
750 °C, H_2-HT	$Ia\bar{3}$	11.0035(9)	3.21
750 °C, H_2-HT+RHT	$Fm\bar{3}m$	5.4831(7)	2.04

[a]Inaccuracies of ±0.1 eV should be considered.
[b]This $Ia\bar{3}$ structure cannot be reverted back to $Fm\bar{3}m$ upon subsequent RHT at lower temperatures.[15,25]

EELS measurements have been performed on the as-synthesized, VHT, and RHT powders. The spectra for Ce and Pr $M_{4,5}$ edges are displayed in Fig. 3. The $M_{4,5}$ white lines in EELS spectra of the rare-earths (REs) result from electronic transitions between the initial state 3*d* and the 4*f* orbitals, such as $3d_{3/2} \rightarrow 4f_{5/2}$ (M_4) and $3d_{5/2} \rightarrow 4f_{7/2}$ (M_5). The relative intensity ratio (I_{M_5}/I_{M_4}) and chemical shift of the $M_{4,5}$ lines denote the change in valency (or the *f*-shell occupancy) of the respective RE cations.[37] The EELS spectra for Ce and Pr are of utmost importance as these two elements exhibit the highest tendency to vary between the 3+ and 4+ states, whereas La, Sm, and Y are known for their stable 3+ electronic configuration. For Ce, two white lines at 882 eV and 902 eV are observed, which are related to M_5 and M_4 transitions, respectively.[37,38] However, no noticeable chemical shifts of these lines have been observed after VHT or RHT. This finding is further supported by the fact that the I_{M_5}/I_{M_4} ratio is relatively invariant with respect to heat treatment [Fig. 3(b)]. Unlike Ce, the scenario is different for Pr. For the as-synthesized system, Pr $M_{4,5}$ white lines are observed at 931 eV and 951 eV, respectively. A significant chemical shift (of ~0.6 eV) toward low energies occurred upon VHT, which indicates a reduction in Pr from a pronounced 4+ state to 3+ dominated multivalent (3+/4+) state.[39] The formation of Pr^{3+} is supported by the pronounced shoulder at the left (or lower energies) of the Pr M_4 line. Additionally, an increase in I_{M_5}/I_{M_4} of Pr is also observed upon VHT, further confirming the decrease in Pr^{4+} [Fig. 3(b)]. Likewise, upon subsequent RHT of the VHT sample in air, a reverse behavior, i.e., an oxidation of Pr toward the initial Pr^{4+} dominated mixed valence state, could be observed.

The reduction of Pr with VHT should be compensated internally. One way of charge compensation can be via oxidation of the other constituent cations, which is not the case here. Hence, the formation of oxygen vacancies can be expected. We have utilized Raman spectroscopy to study this possibility. Two characteristic

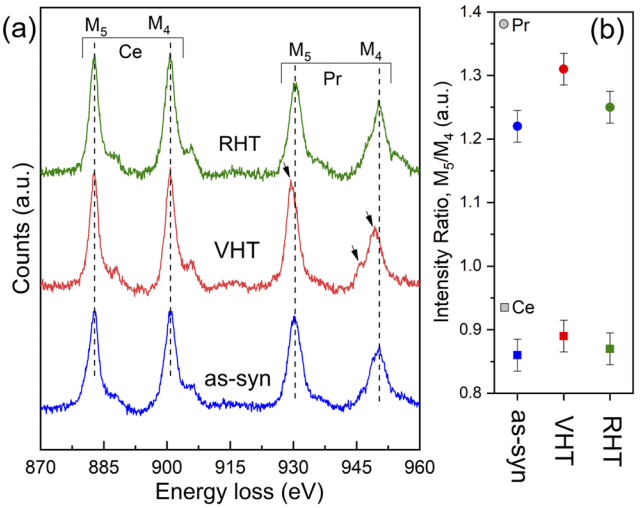

FIG. 3. (a) EELS spectra of the F-HEO showing the Ce and Pr $M_{4,5}$ edges. The chemical shift of Pr edges along with the shoulder at lower energy losses to M_4 indicates the reduction of Pr upon VHT. (b) Average Ce and Pr I_{M_5}/I_{M_4} intensity ratios calculated from (a) indicate the *f*-shell occupancy.

bands centered at ~452 cm^{-1} and ~580 cm^{-1} in all samples are used for the estimation of the V_O concentration (see supplementary material, Fig. SI3). The ~452 cm^{-1} band corresponds to the F_{2g} stretching mode of the fluorite structure, while the latter corresponds to the presence of V_O.[40,41] The integral intensity ratio of V_O to F_{2g} can be used for a relative estimation of the V_O concentration in different systems.[42] The inset of Fig. SI3 of the supplementary material, shows an increase in the amount of V_O concentration upon VHT, while V_O concentrations in the as-synthesized and RHT samples are nearly comparable (see the related discussion in supplementary material, Sec. 1). Although the V_O and the charge state of the elements are interlinked, it should be noted that the bandgap energy in the F-HEO is rather related to the presence of redox-active Pr and its unoccupied 4*f* intermediate band. This has been observed in our earlier report as well, where we compared various F-HEO compositions with varying amount of oxygen vacancies.[25] Nonetheless, we have probed samples using Raman spectroscopy as the change in the V_O concentration upon heat treatment supports the EELS data and indicates the reversible behavior in the F-HEO.

To summarize, we observe a reversible change in the bandgap upon VHT of the F-HEO followed by RHT. The increase in the energy gap upon VHT is expected due to the decrease in the number of unoccupied Pr 4*f* states, as evidenced from the EELS results. The reduction of Pr and resulting increase in V_O also support the increase in the lattice parameter and microstrain upon VHT. Furthermore, the fact that makes the F-HEO unique is the retention of the single-phase fluorite structure even upon VHT. The stability of a fluorite type oxide structure strongly depends on the presence of a 4+ cation, which in a VHT-F-HEO is only Ce and a minor part of Pr. Likewise, the V_O concentration (as shown from Raman spectroscopy) in VHT-$(Ce_{0.2}La_{0.2}Pr_{0.2}Sm_{0.2}Y_{0.2})O_{2-\delta}$ is rather high compared to conventional binary or doped fluorite type oxides, and δ is expected to be ~0.4. To further investigate the impact of stronger reducing atmospheres on physico-chemical features of F-HEO, heat treatment under a hydrogen atmosphere has been carried out.

B. Heat treatment under highly reducing H_2 atmosphere

$(Ce_{0.2}La_{0.2}Pr_{0.2}Sm_{0.2}Y_{0.2})O_{2-\delta}$ has been heat treated under a highly reducing 5% H_2 + Ar atmosphere (H_2-HT), followed by re-heat treatment (RHT) in air. A reversible change in the powder color can be observed after this treatment, as shown in Figs. 4(a)–4(c). Importantly, the change in the bandgap energy is larger than what was observed for VHT, i.e., increasing from 1.93 eV to 3.21 eV [Fig. 4(d)]. RHT of the H_2-HT powder in air leads to reversion of the bandgap to 2.04 eV. This bandgap tailoring of around 60% (~1.3 eV) can be considered as significant, especially given that the change is reversible.

1. Structural analysis and phase composition upon H_2-HT

Figure 5 presents the XRD patterns along with SAED micrographs for the H_2-HT and RHT samples. Rietveld refinements of the XRD patterns are provided in supplementary material, Fig. SI4. Unlike for the as-synthesized and RHT samples, we observe additional peaks in the XRD patterns for the H_2-HT sample. These additional peaks are the superstructure reflections, indicating a structural

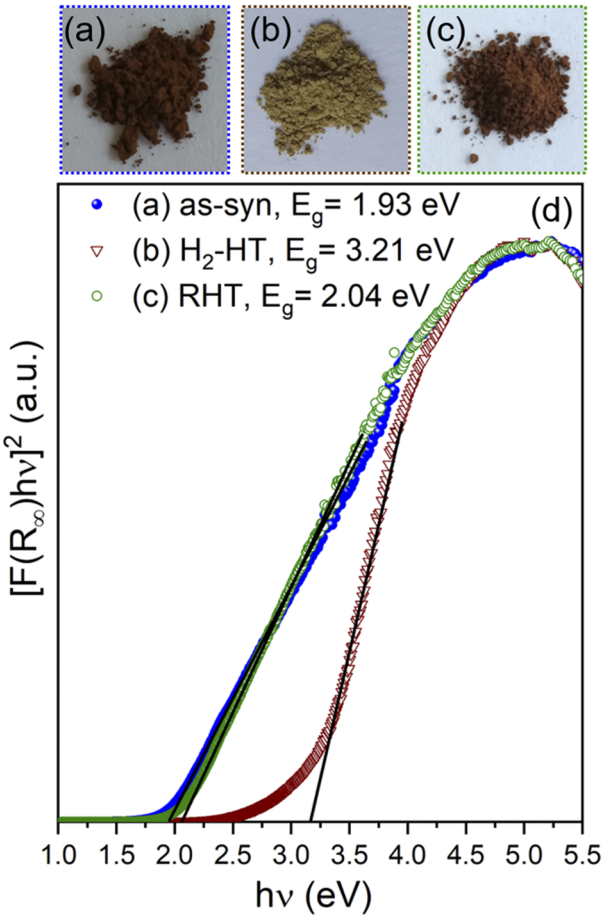

FIG. 4. Photographs (a)–(c) and Tauc plot (d) obtained from the UV-Vis spectra of the $(Ce_{0.2}La_{0.2}Pr_{0.2}Sm_{0.2}Y_{0.2})O_{2-\delta}$ powder, where (a)–(c) correspond to the as-synthesized, hydrogen heat treated (H_2-HT), and re-heat treated samples, respectively. The bandgap values are within the 5% error bar, i.e, ±0.1 eV.

transition from a fluorite ($Fm\bar{3}m$) to C-type bixbyite ($Ia\bar{3}$) structure. Evidence of faint superstructure reflections can also be observed in the SAED pattern (Fig. 5), which further confirms the formation of the bixbyite structure. Homogeneous cationic distribution, down to the nanometer length scales, further supports the phase purity of the bixbyite formed upon H_2-HT (supplementary material, Fig. SI5).

Bixbyite is a well-known low symmetry oxygen deficient body centered cubic variant of the fluorite family, where one out of every four oxygen ions is missing.[43,44] The symmetry relationship between fluorite (*a*) and bixbyite (2*a*) includes a twofold increase in the lattice parameter. Thus, for direct structural comparisons, the pseudosymmetric lattice parameter of the bixbyite structure (i.e., half of the actual lattice parameter) is considered. In fact, the as-synthesized $(Ce_{0.2}La_{0.2}Pr_{0.2}Sm_{0.2}Y_{0.2})O_{2-\delta}$ sample undergoes a similar symmetry lowering when heat treated in normal atmospheric conditions (i.e., under air).[15,25] However, there are two subtle differences between the symmetry lowering happening upon normal heat

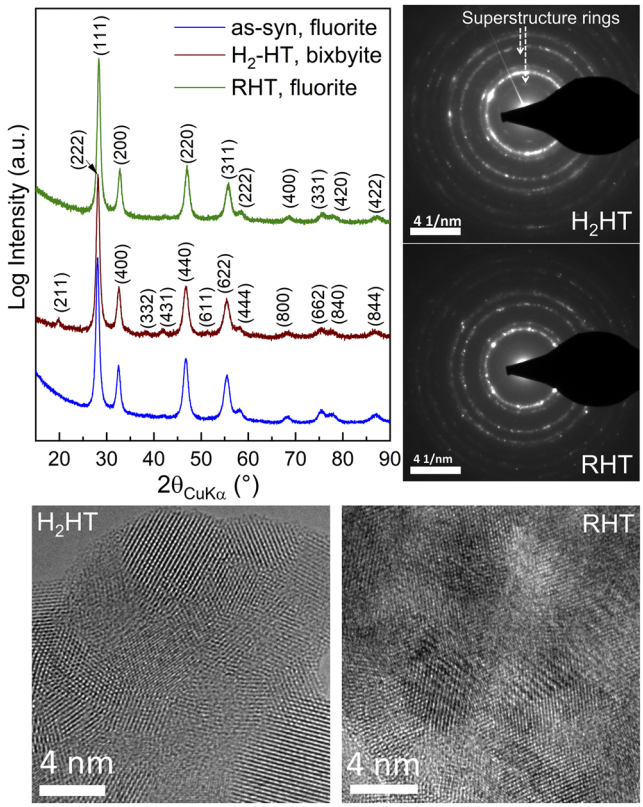

FIG. 5. A reversible transition from a fluorite to bixbyite structure is observed upon hydrogen heat treatment (H_2-HT) followed by air re-heat treatment of $(Ce_{0.2}La_{0.2}Pr_{0.2}Sm_{0.2}Y_{0.2})O_{2-\delta}$. The TEM micrographs and SAED patterns confirm the reversible disorder–order type structural transition.

treatment in air (as observed in our earlier studies) and the H_2-HT. First of all, upon H_2-HT, this phase transition happens at a much lower temperature, i.e., already at 750 °C, whereas the phase transition will happen only above 1000 °C if heat treated under a normal air atmosphere.[15,25] Second and a rather unusual phenomenon is that the phase transition to bixbyite upon H_2-HT is reversible, i.e., a single-phase fluorite structure can be regained when the H_2-heat treated sample is re-heated (RHT) in air at 750 °C (see XRD and SAED in Fig. 5). However, we observed[15,25] that the transition to a bixbyite phase is completely irreversible if the as-synthesized sample is heat treated above 1000 °C in a normal air atmosphere.[15,25] As mentioned above, the transition from fluorite to bixbyite is mostly governed by the presence of oxygen vacancies, which start to order above a certain temperature. One of the reasons for the structural transition already at 750 °C upon H_2-HT can be the formation of additional oxygen vacancies due to a stronger reducing atmosphere. This is supported by an increase (~0.5%, Table I) in the pseudosymmetric lattice parameter upon H_2-HT. In fact, 750 °C under H_2 might already be sufficient to order the oxygen vacancies. However, the temperature might still not be large enough to result in a stable ordering, making the transition back to fluorite upon RHT possible. Further discussion of this point is presented in Sec. III C.

Table I summarizes the structural and optical features obtained upon various heat treatments of F-HEOs.

We have used Raman spectroscopy to further investigate these systems due to its sensitivity to local chemical changes, especially related to light scatterers such as oxygen. It should be noted that the infrared laser, which we typically use to study the F-HEO, could not be used for the H_2-HT sample due to possible resonance effects (see supplementary material, Fig. SI6). Hence, a green laser (λ = 532 nm) has been used for comparison. It is shown in Fig. 6 that all the F-HEO systems show distinct Raman bands at ~452 cm^{-1}, ~1180 cm^{-1}, and ~580 cm^{-1}. By comparing these with the parent binary (or doped) rare-earth based oxides (containing Ce/La/Pr/Sm/Y), we can draw correlations with CeO_2 based systems.[40,42,45–47] The band at ~452 cm^{-1} can be associated with the triply degenerated F_{2g} vibration mode.[41] The band at ~1180 cm^{-1} can be related to the second order 2*LO* Raman mode, which is generally observed in ceria or its doped variants.[40,41] The strong broad band at ~580 cm^{-1} can be best fitted using a two band model, which can be attributed to the presence of oxygen vacancies (V_O) and its related bonding with the 3+ and 4+ cations.[45] Given the fact that bixbyite (as in H_2-HT) is a superstructure of fluorite, additional vibration bands or strengthening/rupturing of some existing ones can be expected. After H_2-HT, three additional bands appear. The band at ~358 cm^{-1} [Fig. 6(a)] can be attributed to a second order Raman mode arising from a combination of A_{1g}, E_g, and F_{2g} scattering tensors.[40] However, we do not find a proper match for the two

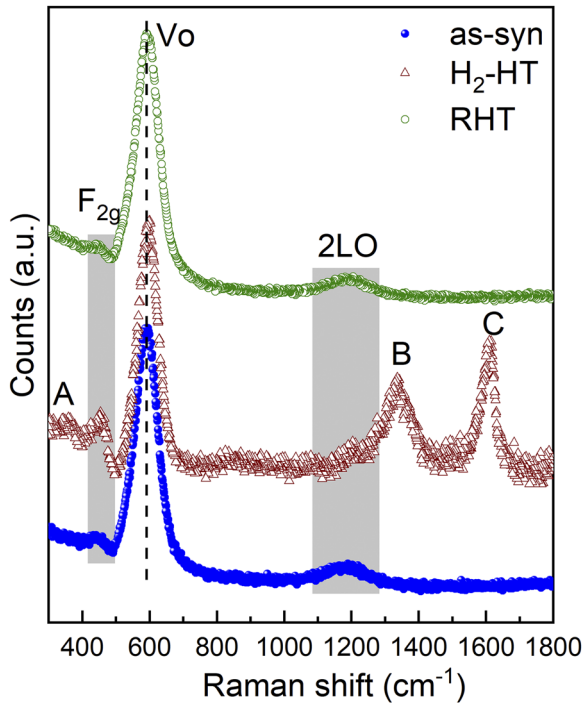

FIG. 6. Raman spectra of $(Ce_{0.2}La_{0.2}Pr_{0.2}Sm_{0.2}Y_{0.2})O_{2-\delta}$ using the 532 nm excitation laser. Three additional bands centered at 358 cm^{-1} (a), 1333 cm^{-1} (b), and 1610 cm^{-1} (c) are observed in the H_2-HT system.

prominent additional bands at ~1333 cm^{-1} and ~1610 cm^{-1}, which are observed only upon H_2-HT (see Fig. 6). Furthermore, these bands cannot be directly attributed to the crystal structural change as the bixbyite variant of $Ce_{0.2}La_{0.2}Pr_{0.2}Sm_{0.2}Y_{0.2})O_{2-\delta}$ obtained upon normal air heat treatment does not exhibit these features (see the Raman spectra in supplementary material, Fig. SI7). Interestingly, both the bands disappear upon subsequent RHT of the H_2-HT sample in air, and a spectrum similar to the as-synthesized system is obtained. One of the plausible reasons for the appearance of the additional bands upon H_2-HT can be due to possible hydrogen incorporation in the F-HEO system. Hydrogen being a light element can lead to strong vibrational modes. Recently, it has been reported that H incorporation (even in the hydride form) is possible in the (bulk) fluorite type CeO_2 when it is heat treated above 350 °C in a H_2 atmosphere.[48] Such a H-incorporation cannot be ignored in the F-HEO as H_2-HT is done at 750 °C. Moreover, the presence of large V_O concentrations in the F-HEO might potentially facilitate H-incorporation. However, this is a speculation and finding concrete evidence of the presence of H is not simple. Hence, experiments sensitive to H, such as inelastic neutron scattering, are needed to support such a hypothesis.

In order to further understand the other physico-chemical changes happening upon H_2-HT, XAS has been performed.

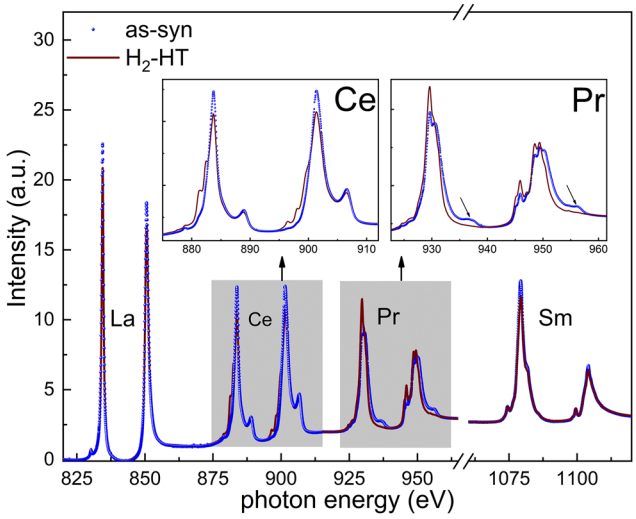

FIG. 7. XAS spectra at the different RE $M_{4,5}$ edges for the as-synthesized and H_2-heat treated sample. The respective spectrum has been normalized to the edge jump after the M_4 edge. The insets show a magnification of the Ce and Pr edges.

C. Element resolved charge state and electronic structure of F-HEO

XAS probes the (unoccupied) electronic density of states above the Fermi energy in an element specific way.[36,49] Hence, it offers the possibility to disentangle the element specific contributions in complex systems such as F-HEOs. Each of the XAS spectra has been normalized to the edge jump. In the following, the respective changes at the different absorption edges are discussed. In addition, an investigation concerning changes in the amount of unoccupied states has been performed.[50,51]

1. Rare-earth $M_{4,5}$ edges: 3d → 4f and L_3 edge: 2p → 5d

At the $M_{4,5}$ edges, the transition from the 3*d* states into the unoccupied 4*f* states occurs (in a dipole approximation). The respective absorption spectra for the as-synthesized and H_2-HT sample are shown in Fig. 7. The La $M_{4,5}$ edges indicate that both the as-synthesized and H_2-HT samples are in the 3+ valence state, while a reduction in the free states by ~3.5% can be determined by the difference of the integrated spectral area. We see a similar, intuitive behavior for Sm, which is also in a 3+ valence state in both cases, while the integrated spectral area is reduced by 3.9% upon H_2-HT. For Ce, a detailed fine structure occurs prior to both the M_5 and M_4 edges after H_2-HT (inset of Fig. 7). These additional peaks can be assigned to Ce^{3+}, while the initial peaks can be assigned to Ce^{4+}.[52,53] Therefore, it can be said that Ce is present in a 4+ dominated multivalent (3+/4+) state after H_2-HT. Due to the occurring multivalency in Ce, a change in the number of unoccupied states can only be determined from the integrated spectrum. From this analysis, an increase of 0.9% of the integrated white line intensity can be determined—such an increase can be neglected and can be explained by differences in the normalization procedure. Pr, on the other hand, is present in a multivalent 3+/4+ state (with a pronounced 4+ nature), as indicated by the prominent after edges[54] in the as-synthesized sample (see the inset of Fig. 7). It changes into a (fully) 3+ state upon H_2-HT. Furthermore, the unoccupied 4*f* states in Pr are reduced by ~15%.

Furthermore, the RE L_3 edges are also studied as the hard x rays in the transmission mode provide a better idea about the bulk nature of the sample. In the L_3 edge, the transition from the $2p_{3/2}$ states to unoccupied 5*d* states occurs. Ce and Pr L_3 spectra are shown in Fig. 8. A complete spectrum including La and Sm is provided in supplementary material, Fig. SI8. For the L_3 absorption edge, the discussion is simpler compared to the $M_{4,5}$ edges. For La and Sm, a 3+ state is evident, while no significant change in the white line intensity is visible. For Ce, a 4+ state can be observed in the as-synthesized sample, while a reduction to a mixed valent state is evident upon H_2-HT. The presence of Ce^{3+} results in shoulder A,[47] as shown in the inset of Fig. 8. Nevertheless, a pronounced Ce^{4+} state is maintained even upon H_2 with no major change in the white line intensity. For Pr, a significant change in the spectral structure is visible. The as-synthesized sample shows a distinct multiplet spectrum ($4f^2$ and $4f^1$ in the inset of Fig. 8). From the literature, it is known that such a spectrum is typically observed in multivalent $Pr^{3+/4+}$, where Pr^{4+} is ascribed to the $4f^1$ peak.[55,56] After H_2-HT, the change in the spectral near-edge fine structure indicates a complete reduction to Pr^{3+}. Accompanied with this change is a reduction in the spectral area by ~3%. This can be explained either by a change in the unoccupied 5d states or structural changes due to the EXAFS signal from the La L_2 edge ($E_{0,La\,L_2}$ = 5891 eV). For this, a detailed EXAFS modeling would be necessary, which is difficult due to the relatively small available *k*-space for this complex system, as visible in supplementary material, Fig. SI8.

The mild reduction of Ce and strong reduction of Pr are in good agreement with the crystal structural transition to bixbyite observed upon H_2-HT. Ce^{4+} is known to play a pivotal role in stabilizing the

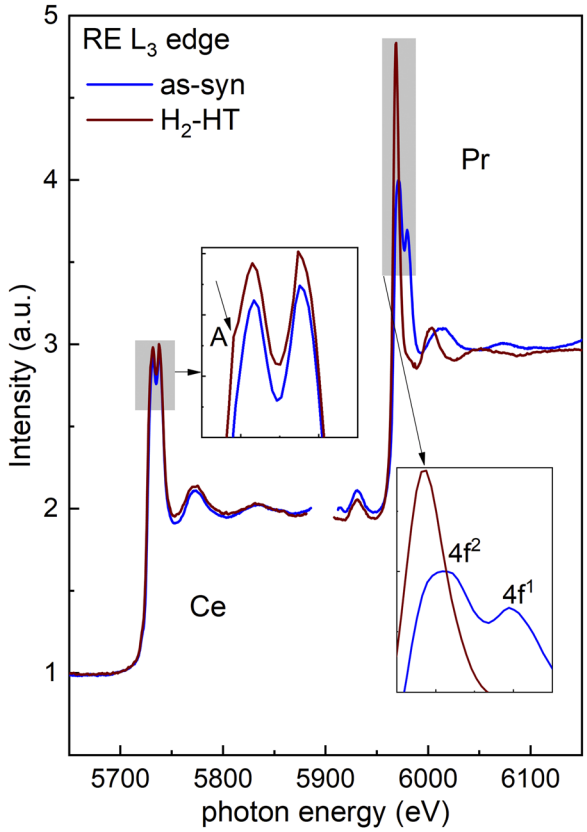

FIG. 8. XAS spectra at the Ce and Pr L_3 edges for the as-synthesized and H_2-heat treated samples. The peak for E = 5930 eV originates from the La L_2 edge.

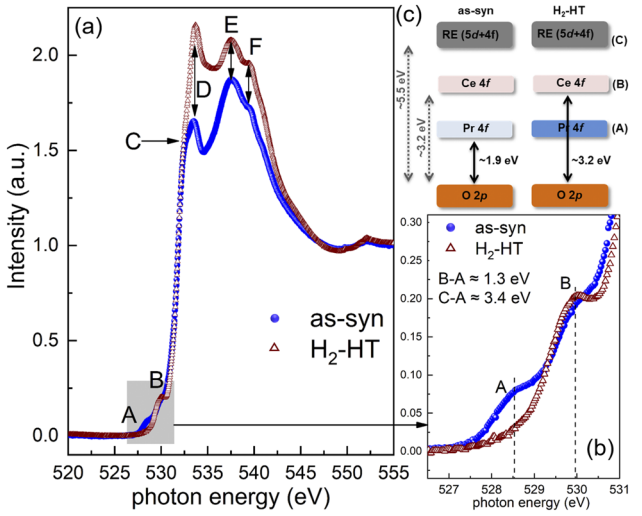

FIG. 9. (a) O K edge XAS spectra of the as-synthesized and H_2-heat treated sample. The spectra are normalized to the edge jump. (b) Magnification of the pre-edge region. (c) Schematic of the electronic band diagram of as-synthesized (oxidized) and H_2-heat treated (reduced) F-HEOs.

fluorite lattice in F-HEOs.[15,25] Thus, even the mild reduction of Ce^{4+} most likely destabilizes the fluorite lattice. The accompanying strong reduction of Pr along with the presence of other 3+ cations leads to an enhanced V_O concentration. Hence, oxygen vacancy ordering (see Sec. III C 2) can be triggered at relatively lower temperatures (750 °C) compared to normal air heat treatment (1000 °C). As mentioned in Sec. III B 1, the ordering upon H_2-HT is most likely metastable, given the intensities of the superstructure reflections are rather weak (Fig. 5 and supplementary material, Fig. SI4) compared to XRD patterns of bixbyite obtained from air-heat treatment.[15,25] Thus, upon RHT, the fluorite structure can be regained.

2. Oxygen K-edge: 1s → 2p

Finally, we focus on the hybridization of the O 2p states with the RE neighbors by probing the O 1s → 2p transition at the O K edge. Unlike the RE cations, the XANES spectrum of the O K edge is rather complex as O hybridizes with all RE cations. Hence, disentangling all spectral features is not straightforward, given the fact that XANES of the F-HEO (or similar complex systems) has not been reported on before. Nevertheless, the changes happening in the RE $M_{4,5}$ and L_3 edges help us to identify the major spectral variation in O K edges upon heat treatment. The prominent features are observed at the photon energy E = 528.6 eV (A), 530 eV (B), 532 eV (C), 533 eV (D), 537 eV (E), and 539 eV (F), respectively (see Fig. 9). Feature A can be attributed to the Pr 4f-O 2p hybridization[27] (discussion pertaining to this feature is explained in Sec. IV). Features B, D, and E have been attributed to O 2p states, which hybridize with the 4f, 5d-e_g, and 5d-t_{2g} levels of Ce in stoichiometric CeO_2, respectively.[27,57] The splitting of the 5d–e_g and 5d–t_{2g} states occurs only if crystal field effects lift the degeneracy,[57,58] indicating that the changes in spectral features D and E are due to an alteration of the local structure (evident from Fig. 5). The relative increase in the peak intensity of feature D compared to feature E reveals a local ordering of the oxygen vacancies. This finding is in agreement with reports on doped CeO_2[38,44] and supports the formation of the C-type bixbyite structure upon H_2-HT. Feature F (539 eV) can be matched with the O 2p and Sm 5d hybridization[59,60] and hence does not change upon H_2-HT. Likewise, the presence of feature C can also be observed both in the as-synthesized and H_2-HT systems, which is possibly linked to the O 2p-RE 5d hybridization.

IV. DISCUSSION

In conventional rare-earth (RE) oxides, the occupied oxygen 2p states are hybridized with RE 5d/4f states, resulting in the formation of the bonding and anti-bonding orbitals. The O 2p state with the occupied RE 5d/4f state forms the valence band, which is generally classified as the O 2p band. However, the anti-bonding states originating from the RE-O hybridization are the conduction bands, which are generally denoted in terms of the RE state related to the specific hybridization, such as RE 5d/4f. Thus, the electronic transition from the O 2p state to the unoccupied RE 5d/4f states determines the bandgap energy. In fact, the changes in the electronic structure of binary rare-earth oxides can be directly correlated with the changes observed in O K edges.[60] Likewise, in the

case of the F-HEO, the analysis of the O *K* XANES edge provides a comprehensive understanding of the electronic band structure and valence states (which is also supported by the other spectroscopic techniques). The most interesting features in the O *K* edge of F-HEOs are A and B. As mentioned above, feature B corresponds to the Ce 4*f*-O 2*p* hybridization, while feature A corresponds to the Pr 4*f*-O 2*p* hybridization. Feature B is present in both cases; however, the intensity of feature A decreased to almost zero after H_2-HT. This indicates distinct changes in Pr 4*f* states that are related to the reduction in Pr valency or decrease in the unoccupied states in the 4*f* level (see Pr-$M_{4,5}$ edges in Fig. 7). Here, we would like to mention that the bandgap energy difference (see Fig. 4) between the as-synthesized sample and the H_2-HT sample is ~1.3 eV. This value matches almost perfectly the energy difference between feature A (Pr 4*f*-O 2*p*, 528.6 eV) hybridization and feature B (Ce 4*f*-O 2*p*, 529.9 eV) hybridization. The weakening of feature A means an increase in the occupation of the Pr 4*f* band, thus prohibiting electronic transitions to the same. This finding validates our band energy diagram [see Fig. 9(c)], where we expect that the electronic transitions will occur from the O 2*p* state (valence bands) to Pr 4*f* (unoccupied) state in the case of the as-synthesized system. However, upon reduction of Pr, the 4*f* level will get filled; hence, the transition to unoccupied Ce 4*f* will determine the bandgap. This is exactly what we observed in the O *K* edge [see Fig. 9(c)] when the as-synthesized and the H_2-HT systems were compared. The fact that feature B becomes prominent upon H_2-HT, even upon the reduction of Ce^{4+}, can be explained as follows: First, the reduction of Ce^{4+} to Ce^{3+} is rather mild as the predominance of Ce^{4+} can be observed from the Ce $M_{4,5}/L_3$ edges (Figs. 7 and 8). Additionally, no major changes in the white line intensity of Ce $M_{4,5}$ indicate only negligible changes in the Ce 4*f* occupancy.

Furthermore, as shown in Fig. 9(a), both the Pr 4*f*-O 2*p* and the Ce 4*f*-O 2*p* hybridization are actually pre-edge features, while the main absorption corresponding to the RE 5*d*-O 2*p* hybridization starts above 531 eV. This is equivalent to our hypothesized energy band diagram [Fig. 9(c)] with the two intermediate energy bands at lower energy gaps, while the gap between O 2*p* and unoccupied RE 5*d* is much larger. The energy difference between features A and C is ~3.5 eV (so is the energy difference between the onset of edge A to edge C). This means that the effective gap between O 2*p* and RE 5*d* is ~5.5 eV. In fact, this value is in good agreement with our earlier hypothesis[25] and is close to the expected energy gap in rare-earth oxides without intermediate 4*f* states.[26,60] Hence, it can be summarized that in F-HEOs, Ce and Pr lead to the formation of intermediate energy states, resulting in narrow bandgaps, whereas the other 3+ cations add to the main energy gap of ~5.5 eV. Depending upon the heat treatment condition, i.e., reducing/oxidizing atmospheres, each of these electronic structures in F-HEOs can be achieved reversibly.

V. CONCLUSIONS

This work attempts to provide a comprehensive understanding of the tunable electronic band structure in a fluorite type rare-earth based high entropy oxide (F-HEO). Owing to the element specific techniques used here, it is possible to disentangle the individual effects of the constituent cations, which can be directly correlated to the observed reversible changes in the optical features. Reversible changes (~0.5 eV) in the bandgap energies are achieved in the F-HEO upon vacuum heat treatment followed by reheating in air. Importantly, the single-phase fluorite type structure of $(Ce_{0.2}La_{0.2}Pr_{0.2}Sm_{0.2}Y_{0.2})O_{2-\delta}$ is maintained even upon vacuum heat treatment with Ce being the sole element, which is purely 4+. This shows the potential of the F-HEO to accommodate a large amount of oxygen vacancies. A stronger reduction of F-HEO, achieved via hydrogen heat treatment, allows for a larger change (~1.2 eV) in the bandgap energy, which can be reverted back to the initial state upon subsequent annealing in air. In addition, a reversible structural transition from fluorite to a single-phase oxygen vacancy ordered C-type bixbyite structure has been observed. Raman spectroscopy further strengthens this reversible behavior as local chemical features before and after reheat treatment are identical. X-ray absorption near-edge spectra (XANES), using soft and hard x rays, indicate that the crystal structure transition can be correlated to the reduction of Ce^{4+}, while tuning of the bandgap energy is related to the reduction of Pr and related changes in the Pr 4*f*-O 2*p* hybridization.

Although practical applications using the F-HEO are yet to materialize, the unique combination of narrow and tunable bandgap energies along with large concentrations of oxygen vacancies in the F-HEO might be beneficial for applications related to mixed electronic–ionic conduction, catalysis, etc. In this context, understanding the exact nature of oxygen vacancy ordering and the related fluorite to bixbyite transition is important. Hence, comprehensive high temperature investigations (above 750 °C) under different atmospheres will be crucial. An electrochemical approach to tune the bandgap in the F-HEO can be another prospective research direction. In any case, further experiments and most importantly support from theoretical studies are essential to exploit the complete potential of the F-HEO.

SUPPLEMENTARY MATERIAL

The supplementary material includes the Rietveld refinements of the XRD patterns, TEM–EDS maps, Raman spectra (of vacuum heat treated F-HEO and bixbyite HEO), and XANES of La and Sm L_3 edges.

ACKNOWLEDGMENTS

A.S. and H.H. acknowledge financial support from the Deutsche Forschungsgemeinschaft (DFG) under Project No. HA 1344/43-1. B.E. and H.W. acknowledge financial support from the Deutsche Forschungsgemeinschaft (DFG) under Project No. WE 2623/14-1. X.M. and L.V. acknowledge the support of Karlsruhe Nano Micro Facility (KNMF) for the access to the TEM. A.S. thanks Soumabha Bag (INT, KIT) for fruitful discussions. We thank the Helmholtz-Zentrum Berlin for the allocation of beamtime at the beamline UE46 PGM_1 (Proposal No. 192-08578-ST/R) and Eugen Weschke for the support during the beamtime. We acknowledge DESY (Hamburg, Germany), a member of the Helmholtz Association, for the provision of experimental facilities. Parts of this research were carried out at PETRA III (Proposal No. 20190485), and we would like to thank Ruidy Nemausat for assistance in using the beamline P65. We acknowledge support by the KIT-Publication Fund of the Karlsruhe Institute of Technology.

DATA AVAILABILITY

The data that support the findings of this study are available within the article and its supplementary material.

REFERENCES

[1] C. M. Rost, E. Sachet, T. Borman, A. Moballegh, E. C. Dickey, D. Hou, J. L. Jones, S. Curtarolo, and J.-P. Maria, Nat. Commun. **6**, 8485 (2015).
[2] N. Dragoe and D. Bérardan, Science **366**, 573 (2019).
[3] A. Sarkar, Q. Wang, A. Schiele, M. R. Chellali, S. S. Bhattacharya, D. Wang, T. Brezesinski, H. Hahn, L. Velasco, and B. Breitung, Adv. Mater. **31**, 1806236 (2019).
[4] A. Sarkar, L. Velasco, D. Wang, Q. Wang, G. Talasila, L. de Biasi, C. Kübel, T. Brezesinski, S. S. Bhattacharya, H. Hahn, and B. Breitung, Nat. Commun. **9**, 3400 (2018).
[5] J. Dabrowa, M. Stygar, A. Mikuła, A. Knapik, K. Mroczka, W. Tejchman, M. Danielewski, and M. Martin, Mater. Lett. **216**, 32 (2018).
[6] J. Gild, M. Samiee, J. L. Braun, T. Harrington, H. Vega, P. E. Hopkins, K. Vecchio, and J. Luo, J. Eur. Ceram. Soc. **38**, 3578 (2018).
[7] B. Musicó, Q. Wright, T. Zac Ward, A. Grutter, E. Arenholz, D. Gilbert, D. Mandrus, and V. Keppens, Phys. Rev. Mater. **3**, 104416 (2019).
[8] N. Qiu, H. Chen, Z. Yang, S. Sun, Y. Wang, and Y. Cui, J. Alloys Compd. **777**, 767 (2019).
[9] M. P. Jimenez-Segura, T. Takayama, D. Bérardan, A. Hoser, M. Reehuis, H. Takagi, and N. Dragoe, Appl. Phys. Lett. **114**, 122401 (2019); arXiv:1902.01825.
[10] J. L. Braun, C. M. Rost, M. Lim, A. Giri, D. H. Olson, G. N. Kotsonis, G. Stan, D. W. Brenner, J.-P. Maria, and P. E. Hopkins, Adv. Mater. **30**, 1805004 (2018).
[11] Q. Wang, A. Sarkar, D. Wang, L. Velasco, R. Azmi, S. S. Bhattacharya, T. Bergfeldt, A. Düvel, P. Heitjans, T. Brezesinski, H. Hahn, and B. Breitung, Energy Environ. Sci. **12**, 2433 (2019).
[12] C. Oses, C. Toher, and S. Curtarolo, Nat. Rev. Mater. **5**, 295 (2020).
[13] K. Chen, X. Pei, L. Tang, H. Cheng, Z. Li, C. Li, X. Zhang, and L. An, J. Eur. Ceram. Soc. **38**, 4161 (2018).
[14] L. Spiridigliozzi, C. Ferone, R. Cioffi, G. Accardo, D. Frattini, and G. Dell'Agli, Materials **13**, 558 (2020).
[15] R. Djenadic, A. Sarkar, O. Clemens, C. Loho, M. Botros, V. S. K. Chakravadhanula, C. Kübel, S. S. Bhattacharya, A. S. Gandhi, and H. Hahn, Mater. Res. Lett. **5**, 102 (2017).
[16] B. Cheng, H. Lou, A. Sarkar, Z. Zeng, F. Zhang, X. Chen, L. Tan, V. Prakapenka, E. Greenberg, J. Wen *et al.*, Commun. Chem. **2**, 114 (2019).
[17] D. Bérardan, S. Franger, A. K. Meena, and N. Dragoe, J. Mater. Chem. A **4**, 9536 (2016).
[18] R. Witte, A. Sarkar, R. Kruk, B. Eggert, R. A. Brand, H. Wende, and H. Hahn, Phys. Rev. Mater. **3**, 34406 (2019).
[19] H. Chen, J. Fu, P. Zhang, H. Peng, C. W. Abney, K. Jie, X. Liu, M. Chi, and S. Dai, J. Mater. Chem. A **6**, 11129 (2018).
[20] J. Zhang, J. Yan, S. Calder, Q. Zheng, M. A. Mcguire, D. L. Abernathy, Y. Ren, S. H. Lapidus, K. Page, H. Zheng, J. W. Freeland, J. D. Budai, and R. P. Hermann, Chem. Mater. **31**, 3705 (2019).
[21] P. B. Meisenheimer, T. J. Kratofil, and J. T. Heron, Sci. Rep. **7**, 13344 (2017).
[22] D. Wang, Z. Liu, S. Du, Y. Zhang, H. Li, Z. Xiao, W. Chen, R. Chen, Y. Wang, Y. Zou, and S. Wang, J. Mater. Chem. A **7**, 24211 (2019).
[23] Y. Sharma, Q. Zheng, A. R. Mazza, E. Skoropata, T. Heitmann, Z. Gai, B. Musico, P. F. Miceli, B. C. Sales, V. Keppens, M. Brahlek, and T. Z. Ward, Phys. Rev. Mater. **4**, 014404 (2020).
[24] R. K. Patel, S. K. Ojha, S. Kumar, A. Saha, P. Mandal, J. W. Freeland, and S. Middey, Appl. Phys. Lett. **116**, 071601 (2020).
[25] A. Sarkar, C. Loho, L. Velasco, T. Thomas, S. S. Bhattacharya, H. Hahn, and R. Djenadic, Dalton Trans. **46**, 12167 (2017).
[26] R. Gillen, S. J. Clark, and J. Robertson, Phys. Rev. B **87**, 125116 (2013); arXiv:1208.0503.
[27] S. G. Minasian, E. R. Batista, C. H. Booth, D. L. Clark, J. M. Keith, S. A. Kozimor, W. W. Lukens, R. L. Martin, D. K. Shuh, S. C. E. Stieber, T. Tylisczcak, and X.-d. Wen, J. Am. Chem. Soc. **139**, 18052 (2017).
[28] L. Petit, A. Svane, Z. Szotek, and W. M. Temmerman, Phys. Rev. B **72**, 205118 (2005).
[29] K. Ahn, D. S. Yoo, D. H. Prasad, H.-W. Lee, Y.-C. Chung, and J.-H. Lee, Chem. Mater. **24**, 4261 (2012).
[30] X. Chen, L. Liu, Z. Liu, M. A. Marcus, W.-C. Wang, N. A. Oyler, M. E. Grass, B. Mao, P.-A. Glans, Y. Y. Peter *et al.*, Sci. Rep. **3**, 1510 (2013).
[31] Topas V5, General profile and structure analysis software for powder diffraction data, User's Manual (Bruker AXS, Karlsruhe).
[32] J. Tauc, R. Grigorovici, and A. Vancu, Phys. Stat. Sol. **15**, 627 (1966).
[33] E. Weschke and E. Schierle, J. Large-scale Res. Fac. JLSRF **4**, A127 (2018).
[34] E. Welter, R. Chernikov, M. Herrmann, and R. Nemausat, AIP Conf. Proc. **2054**, 040002 (2019).
[35] G. S. Henderson, F. M. F. De Groot, B. J. A. Moulton, F. M. F. D. Groot, and B. J. A. Moulton, Spectrosc. Methods Mineral. Geol. **78**, 75 (2014).
[36] H. Wende, Rep. Prog. Phys. **67**, 2105 (2004).
[37] A. M. D'Angelo, A. C. Liu, and A. L. Chaffee, J. Phys. Chem. C **120**, 14382 (2016).
[38] D. R. Ou, T. Mori, F. Ye, J. Zou, G. Auchterlonie, and J. Drennan, Phys. Rev. B **77**, 024108 (2008).
[39] W. J. Bowman, K. March, C. A. Hernandez, and P. A. Crozier, Ultramicroscopy **167**, 5 (2016).
[40] A. Filtschew, K. Hofmann, and C. Hess, J. Phys. Chem. C **120**, 6694 (2016).
[41] W. H. Weber, K. C. Hass, and J. R. McBride, Phys. Rev. B **48**, 178 (1993).
[42] M. Guo, J. Lu, Y. Wu, Y. Wang, and M. Luo, Langmuir **27**, 3872 (2011).
[43] Y.-M. Chiang, *Physical Ceramics: Principles for Ceramic Science* (John Wiley & Sons, Inc., 1997).
[44] D. R. Ou, T. Mori, F. Ye, T. Kobayashi, J. Zou, G. Auchterlonie, and J. Drennan, Appl. Phys. Lett. **89**, 171911 (2006).
[45] C. Schilling, A. Hofmann, C. Hess, and M. V. Ganduglia-Pirovano, J. Phys. Chem. C **121**, 20834 (2017).
[46] N. Dilawar, S. Mehrotra, D. Varandani, B. V. Kumaraswamy, S. K. Haldar, and A. K. Bandyopadhyay, Mater. Charact. **59**, 462 (2008).
[47] R. Schmitt, A. Nenning, O. Kraynis, R. Korobko, A. I. Frenkel, I. Lubomirsky, S. M. Haile, and J. L. M. Rupp, Chem. Soc. Rev. **49**, 554 (2020).
[48] Z. Wu, Y. Cheng, F. Tao, L. Daemen, G. S. Foo, L. Nguyen, X. Zhang, A. Beste, and A. J. Ramirez-Cuesta, J. Am. Chem. Soc. **139**, 9721 (2017).
[49] J. Stöhr, *NEXAFS Spectroscopy* (Springer, Berlin, Heidelberg, 1992).
[50] B. T. Thole, P. Carra, F. Sette, and G. Van Der Laan, Phys. Rev. Lett. **68**, 1943 (1992).
[51] P. Carra, B. T. Thole, M. Altarelli, and X. Wang, Phys. Rev. Lett. **70**, 694 (1993).
[52] S. Alayoglu, K. An, G. Melaet, S. Chen, F. Bernardi, L. W. Wang, A. E. Lindeman, N. Musselwhite, J. Guo, Z. Liu, M. A. Marcus, and G. A. Somorjai, J. Phys. Chem. C **117**, 26608 (2013).
[53] S. Heyraud, P. E. R. Blanchard, S. Liu, Q. Zhou, B. J. Kennedy, H. E. A. Brand, A. Tadich, and J. R. Hester, J. Phys.: Condens. Matter **25**, 335401 (2013).
[54] J. Herrero-Martín, J. L. García-Muñoz, S. Valencia, C. Frontera, J. Blasco, A. J. Barón-González, G. Subías, R. Abrudan, F. Radu, E. Dudzik, and R. Feyerherm, Phys. Rev. B **84**, 115131 (2011).
[55] J. L. García-Muñoz, C. Frontera, A. J. Barón-González, S. Valencia, J. Blasco, R. Feyerherm, E. Dudzik, R. Abrudan, and F. Radu, Phys. Rev. B **84**, 045104 (2011).
[56] T. Ogier, C. Prestipino, S. Figueroa, F. Mauvy, J. Mougin, J. C. Grenier, A. Demourgues, and J. M. Bassat, Chem. Phys. Lett. **727**, 116 (2019).
[57] J. A. Rodriguez, J. C. Hanson, J.-Y. Kim, G. Liu, A. Iglesias-Juez, and M. Fernández-García, J. Phys. Chem. B **107**, 3535 (2003).
[58] A. V. Soldatov, T. S. Ivanchenko, S. Della Longa, A. Kotani, Y. Iwamoto, and A. Bianconi, Phys. Rev. B **50**, 5074 (1994).
[59] S.-Y. Chen, R.-J. Chen, W. Lee, C.-L. Dong, and A. Gloter, Phys. Chem. Chem. Phys. **16**, 3274 (2014).
[60] A. B. Altman, J. I. Pacold, J. Wang, W. W. Lukens, and S. G. Minasian, Dalton Trans. **45**, 9948 (2016).